PHYSICAL REVIEW B **104**, 104107 (2021)

Anomalous thermophysical properties and electride transition in fcc potassium

Long Zhao,[1] Hongxiang Zong,[1,2,*] Xiangdong Ding,[1,†] Jun Sun,[1] and Graeme J. Ackland[2]
[1]*State Key Laboratory for Mechanical Behavior of Materials, Xi'an Jiaotong University, Xi'an, Shanxi 710049, China*
[2]*Centre for Science at Extreme Conditions (CSEC), School of Physics and Astronomy, University of Edinburgh, Edinburgh EH9 3FD, United Kingdom*

(Received 7 July 2021; revised 22 August 2021; accepted 13 September 2021; published 27 September 2021)

Alkali metals undergo an electride transition with excess electrons localized in interstices and acting as anionic interstitial quasi-atoms (ISQs). Less is known about the role of electride transition in changing their thermophysical properties. Here, taking potassium as an example, we investigated the thermodynamic and dynamic properties in the face-centered cubic (fcc) phase region where an electride transition occurs when increasing pressure. With the help of machine-learning-enhanced molecular dynamic simulations and density functional theory calculations, we show property anomalies over a wide pressure range of 10–20 GPa but no accompanying structural transformations. Furthermore, we find that these anomalies in solid potassium are stronger at lower temperatures due to the more electron-localized nature of ISQs. Our findings unveil the rich phenomena in electrides and could deepen our understanding on electride phase transition.

DOI: 10.1103/PhysRevB.104.104107

I. INTRODUCTION

Alkali metals are often considered "simple" metals as their electronic properties can be well described by nearly free-electron models at ambient conditions [1,2]. Under pressure, however, there is growing evidence that alkali metals exhibit many striking phenomena, such as anomalous melting behavior [3–5], the emergence of low-symmetry complex structures [6], and so on [7]. One of the most fascinating ones is the high-pressure electride (HPE) that was first predicted by theoretical models [8] and then confirmed by diamond-anvil cell experiments recently [9]. HPEs differ from traditional electrides in that the thermodynamic reason to form interstitial quasi-atoms (ISQs) is primarily volume reduction, rather than ionicity. HPEs are often metallic, and there is no evidence for paramagnetism [10].

HPEs, in which electrons occupy interstitial regions in crystal and behave as anions, often exhibit unique electromagnetic properties. A pioneering study on Na shows that a pristine metal could become an insulator in the HPE state when suffering from a pressure >200 GPa [9,11,12]. Subsequent experimental and theoretical works also demonstrated that Li transforms into a semiconductor HPE with a gap of 0.3 eV at 80 GPa [13–16]. Simultaneously, the absorption spectrum of Na-HPE is strongly anisotropic, i.e., sodium becomes optically transparent in one direction but reflective in the other ones [11]. Additionally, the reflectivity of both solid and liquid alkali metals (mainly lithium [17] and potassium [18]) shows a slight dip across the electride transition region. Furthermore, it is found that the electron and phonon interaction in HPE state can give rise to an anomalous longitudinal acoustic (LA)-transverse acoustic (TA) splitting in the phonon dispersion [19]. This indicates that an electride transition under high pressure can strongly change the motion of ion cores in solid-phase state, thus the dynamic properties of materials. However, to the best of our knowledge, there are few studies on the thermodynamic or dynamic properties of materials considering the effect of electride transition. Although our recent work on potassium liquid has shown remarkable thermodynamic or dynamic anomalies induced by the atom-to-electride transition, which is accompanied by shape change of local structures [18], it is unclear whether these anomalies accompanying the atom-to-electride transition still exist in the solid-state phase without structural transformation.

Herein, we utilized a machine learning enhanced molecular dynamics (MD) simulation and DFT calculation to explore the thermodynamic and dynamic properties of face-centered cubic (fcc) potassium, which is expected to undergo an atom-to-electride transition under pressure. We note that the evolution of thermodynamic and vibrational properties shows anomalies over a wide pressure range of 10–20 GPa. These abnormalities are derived from the electride transition instead of the structural transformation. Furthermore, we find that these anomalies in the solid state are stronger at lower temperatures due to the more electron-localized nature of ISQs. To this end, we modified the phase diagram of solid potassium in the fcc stable region.

II. METHODS

A domain knowledge-based machine learning approach was adopted to match the true potential energy surface of potassium [18,20,21]. The first-principles calculations of potassium can capture well the phase stability and physical properties from experimental observation, e.g., more accurate melting points can be achieved via *ab initio* MD (AIMD) simulation of the liquid and solid coexistence [22] (see Fig. 1). Therefore, the machine learning interatomic potential (MLIP) was directly learned from an accurate reference database of first-principles calculations [25] using the Vienna *ab initio* Simulation Package (VASP) [26]. The full database was

---

[*] zonghust@mail.xjtu.edu.cn
[†] dingxd@mail.xjtu.edu.cn

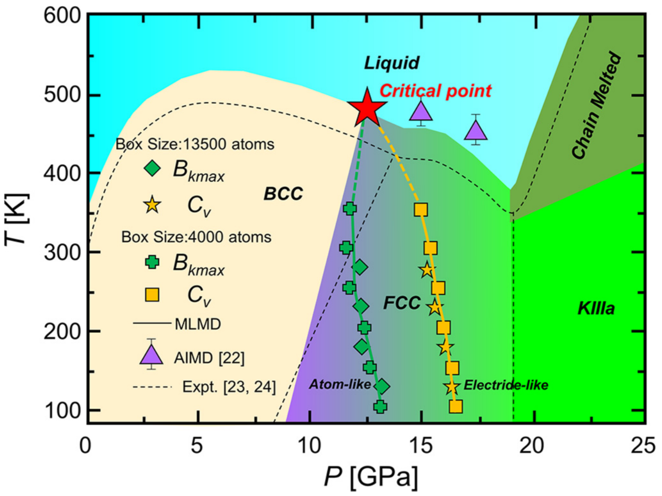

FIG. 1. Phase diagram of potassium as a function of temperature and pressure. The colors present the stability region of different phases. Dash lines are experimental phase boundaries (solid-solid, solid-chain melt, and solid-liquid) taken from Refs. [23,24]. The purple triangles are the melting points detected by *ab initio* molecular dynamics (AIMD) simulations with the solid-liquid coexistence method [22]. Green crossheads (rhombuses) and orange squares (pentagrams) show the maxima of the Debye-Waller factor [$B_k(P)$] and the minima of heat capacity C_V (P) curves at different temperatures, respectively. The critical point here is defined by the crossing of the green and orange lines.

accumulated from the AIMD simulation of body-centered cubic (bcc), fcc, KIIIa, and corresponding liquid structures at different temperatures and pressures. The training dataset and testing dataset were randomly selected from the database with a proportion of 9:1. Then we adopted a linear regression algorithm in which the coefficients were fitted by using the kernel ridge regression method [27]. A more detailed description of this machine learning potential can be found in Ref. [21]. In addition, the performance of MLIP has been evaluated by comparing machine learning prediction with the corresponding density functional theory (DFT) calculations. As shown in Fig. 2, the low mean absolute error (MAE) for both potential energy (∼1.3 meV/atom) and atomic force (∼0.018 eV/Å) suggests a high fidelity of our machine learning potential. This machine learning potential can reproduce well the phase diagram of potassium (see Fig. 1) [18,21], except a slightly vertical shift of the melting curve comparing experimental data. We believe this discrepancy results from the size effect, i.e., the limited size of samples in simulations without considering crystal defects (such as dislocations, grain boundaries, and so on), which can act as heterogeneous nucleation centers of the liquid phase and lower the melting temperatures [28]. In addition, it has successfully been applied to capture the liquid-liquid phase transition (LLPT) induced by electride transitions [18]. Therefore, it allows us to utilize this MLIP to explore the evolution of thermodynamic and dynamic properties in solid potassium across electride phase transition.

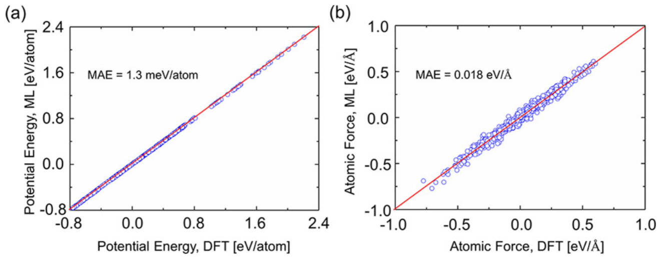

FIG. 2. Performance of our machine learning (ML) potential compared with the density functional theory (DFT) references. (a) Per-atom potential energy and (b) atomic force for configurations. A perfect correlation with the DFT values is shown by the red lines. MAE is the mean absolute error.

Classic MD simulations with a machine learning interatomic potential (hereafter refered to as MLMD) were then performed to study the dynamics of fcc potassium with a time step of 1 fs, and periodic boundary conditions were applied along all three dimensions. MD simulations were run at a fixed density (NVT) with a Nose-Hoover thermostat [29]. All MD simulations were conducted using the LAMMPS package [30], and the atomic configurations were visualized with VESTA [31]. Typical samples of fcc potassium containing up to 4000 atoms were used to study the corresponding thermophysical properties of the solid (such as isothermal bulk modulus B_T, heat capacity C_p, thermal expansion α, and compressibility β) at selected pressures and temperatures. In addition, to eliminate the possible size effect, we also perform MD simulations of larger samples with 13 500 atoms, which show a similar tendency in the pressure dependence of physical properties involved (see Fig. 2).

DFT calculations were performed using VASP [26]. The generalized gradient approximation was used in the scheme of Perdew-Burke-Ernzerhof to describe the exchange-correlation functional [32]. AIMD simulations were utilized in 3×3×3 supercells (with 128 atoms for potassium) with a plane-wave cutoff energy of 450 eV and a denser k-point mesh of 3×3×3. A Nose-Hoover thermostat was used to perform the NVT simulations. For each AIMD simulation, the structure was generated at the appropriate density and held at constant temperatures for 6000 steps with time step of 3 fs. The initial 3 ps were used for the thermalization, and the final 5000 steps of each trajectory were used to extract the statistical quantities. The vibrational density of state (VDOS) at 0 K was calculated using the density functional perturbation theory method as implemented in the PHONOPY package [33], and finite-temperature renormalized VDOS were performed using phonon mode decomposition and the AIMD projection technique implemented in DYNAPHOPY [34]. In addition, analyzing the nonnuclear charge was performed using the Bader partitioning scheme [35] for the charge density. At each pressure, 20 snapshots were averaged for charge density and electron localization function (ELF) [36] calculations.

III. RESULTS

A. Atom-to-electride transition

The proposed atom-to electride transition in potassium was first confirmed by studying the electronic properties at selected temperatures (50 and 150 K) within the fcc stable region (10–20 GPa). Curves of nonnuclear charge maxima and average value counted by Bader analysis [35] are shown

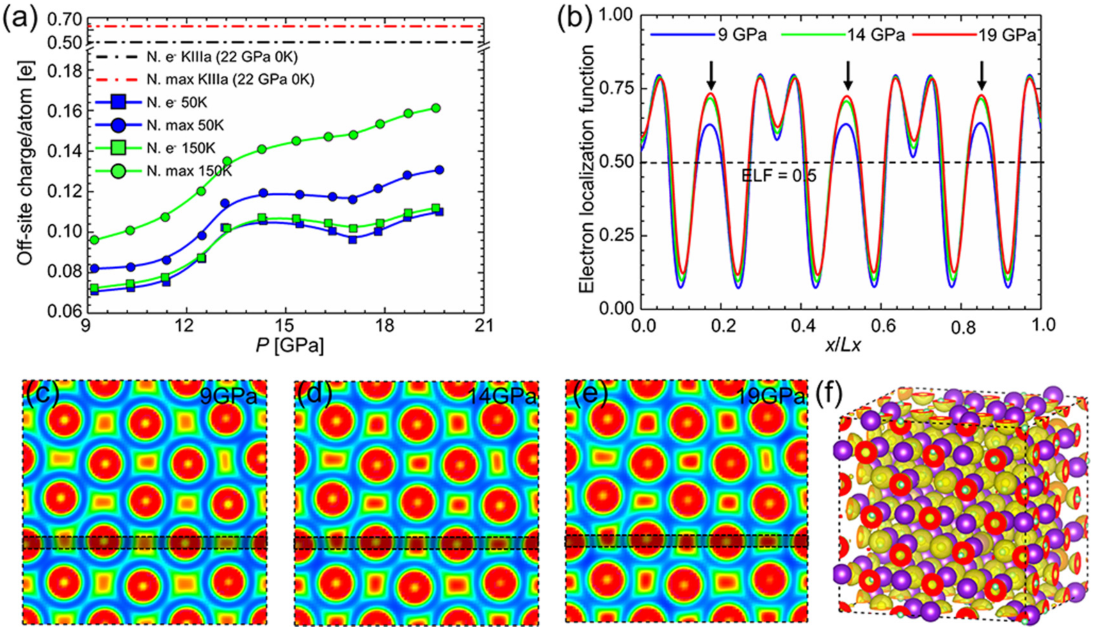

FIG. 3. Electronic properties of face-centered cubic (fcc) potassium as a function of pressure. (a) Frequency of off-atom Bader maxima and average for fcc potassium at 50 K (blue line) and 150 K (green line). (b) Electron localization function (ELF) along the [100] direction. The black arrows point out the center of the nonnuclear charge. (c)–(e) ELF along (001) slices of 50 K data at 9, 14, and 19 GPa, respectively. ELF values are shown in red, green, blue (RGB) scale from 0.0 (blue) to 0.7 (red). (f) *Ab initio* molecular dynamics (AIMD) snapshots of solid potassium (purple), sites of interstitial electron (green), and ELF = 0.7 isosurface (yellow). The N. e$^-$ and N. Max are the average and maximum values of interstitial electrons, respectively.

in Fig. 3(a). At 50 K, both the curves of pressure-dependent maximum and averaged nonnuclear charge are gradually increased from ∼0.06 (at 11 GPa) to ∼0.12 (at 14 GPa) then start to saturate >14 GPa. This indicates that fcc potassium undergoes a transition from an atomiclike state to an electridelike state. Although the nonnuclear charges at both 50 and 150 K show a similar atom-to electride transition, their pressure dependences are different, i.e, the nonnuclear charge at 50 K shows a sharper change than that of 150 K when across the pressure of ∼11–14 GPa, suggesting a temperature effect in fcc potassium. In addition, the average (∼0.5) and maximum (∼0.6) nonnuclear electron of KIIIa at 22 GPa and 0 K were calculated [see the black and red dash line in Fig. 3(a)]. We note that the full electride nature of KIIIa is of higher intensity than the fcc phase (∼ $\frac{1}{5}$ of KIIIa), which indicates the interstitials of the fcc structure are partially filled by the electrons. We plot the change of the ELF along the [100] direction in Fig. 3(b). We note that ELF at interstitial sites is ∼0.73 (>0.5) and gradually increases with the increases of pressure [as pointed out by the black arrows in Fig. 3(b)], consistent with the stronger localized nature of electrons at the interstitial sites upon electride transition. Figures 3(c)–3(e) show the spatial distribution of ELFs at 50 K, which confirms the strong localization of electrons at octahedral interstitial sites. The fcc structure has one such octahedral site per atomic site. The nonnuclear ELF maxima (noncircular red blobs) become more pronounced as we increase the pressure from 9 to 19 GPa, consistent with our Bader analysis in Fig. 3(a). Figure 3(f) relates the Bader and ELF analyses, confirming that the nonnuclear Bader value is associated with the region of localized electrons, i.e., high values of ELF.

Subsequently, we investigated the corresponding structure factor $S(q)$ as a function of pressure in Fig. 4. Here, $S(q)$ is calculated by a Fourier transform of the corresponding radial distribution functions and can be directly measured by diffraction experiments. In Fig. 4(a), $S(q)$ for different

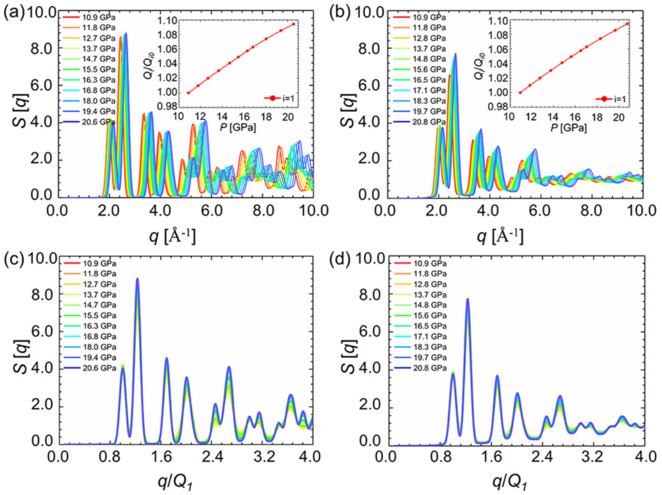

FIG. 4. Structural properties of solid potassium from machine learning molecular dynamics (MLMD) simulations. Structure factor function at selected pressures for (a) 50 K and (b) 250 K. The inset shows the relative location of the first peaks (Q_1/Q_{10}) as a function of pressure [where Q_1 is the location of the first peak in $S(q)$ at selected pressures, while Q_{10} is the reference position of the first peak at 10.9 GPa]. Normalized structure factor function by Q_1 at selected pressures for (c) 50 K and (d) 250 K.

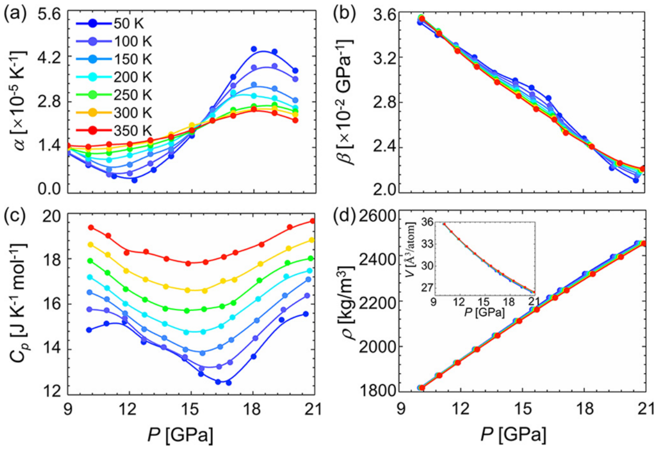

FIG. 5. Thermodynamic properties of solid potassium, shown as a function of pressure for selected temperatures. (a) Thermal expansivity α, (b) compressibility β, (c) heat capacity C_p, and (d) equation of state $\rho(P)$ [the insert shows the $V(P)$].

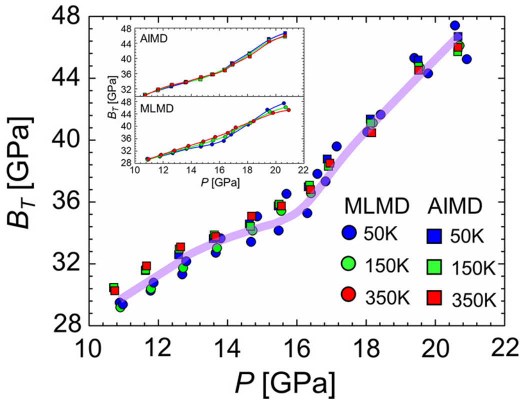

FIG. 6. Comparison of isothermal bulk modulus for machine learning molecular dynamics (MLMD) and *ab initio* molecular dynamics (AIMD) data at 50, 150, and 350 K. The purple line is used to guide the eyes. The insert shows the temperature effect in MLIP and AIMD simulation data.

pressure cases share a similar feature except a slight shift of the peaks, which reflects the structural evolution with volume (density) variance under pressure. To quantify this, we calculated the corresponding Q_1/Q_{10} [where Q_1 is the position of the first peak in $S(q)$ at selected pressures, while Q_{10} is the reference position of the first peak at 10.9 GPa] in the insert of Fig. 4(a), whose pressure dependence shows a continuous nature, indicating the absence of accompanying significant structural change in this pressure region. Furthermore, the evolutions of the normalized structure factors by Q_1 at selected pressures for both 50 and 250 K are shown in Figs. 4(c) and 4(d) (Q_1 is the position of the first peak of the structure factor functions). Interestingly, all the peaks at different pressures almost exactly coincide, lending credence to the occurrence of pressure-induced isostructure transition. Furthermore, different from the electronic properties shown in Fig. 3, the structural motif shows no temperature dependence, as demonstrated by comparing $S(q)$ of 50 and 250 K in Fig. 4. Therefore, fcc potassium in this pressure region can serve as an ideal testbed for us to focus on the effect of the atomlike-to-electridelike transition on the thermodynamic or dynamic properties of solid phases under high pressure.

B. Thermodynamic properties

Figure 5 shows the thermal expansivity α, compressibility β, heat capacity C_p, and density of state (EOS) as a function of pressure. The thermal expansion coefficient α was first calculated in Fig. 5(a), and systematic observation in different temperature data demonstrates an anomalous behavior. The thermal expansion curves have local maxima and minima in this pressure region with a strong dip between 9 and 12 GPa. The dip is gradually weakened as the temperature rises, which is consistent with the electrical resistance evolution upon heating at 13 GPa [24]. The same anomaly is true for the compressibility β and the heat capacity C_p, i.e., fcc potassium is more compressible but has lower heat capacity in the pressure crossover region at low temperatures (<300 K), see Figs. 5(b) and 5(c). It is important to point out that these anomalies gradually disappeared at high temperatures (>350 K but below melting point). We note that the region of all these thermodynamic anomalies is almost consistent with the atom-to-electride transition regime in Fig. 3(a). In addition, to explore the effect of electride transition, we checked the EOS by calculating the corresponding pressure dependence of density. However, we see no measurable density discontinuity along the EOS curves [see Fig. 5(d)]. It suggests that this is a continuous phase transition, like what we have found in the high-temperature region with a LLPT [18].

To check the reliability of the MLMD simulation result, the MLMD and AIMD data of the isothermal bulk modulus, related to density by $B_T = \rho(\partial P/\partial \rho)_T$, including 50, 150, and 350 K, are compared in Fig. 6. Both data show a similar tendency in the pressure dependence of B_T, and a clear bump occurs at ~16 GPa, which indicates the remarkable change of slope in the B_T curve. This is concordant with the other thermodynamic anomalies (α, β, and C_p) in Fig. 5. Also, a similar B_T anomaly has been observed in dense potassium liquid [18] and rubidium liquid [37]. This consistency indicates the reliability of our MLMD simulation results, i.e., the anomalies of thermodynamic properties indeed exist in fcc potassium, consistent with the presence of an electride transition in the region of 10–20 GPa. Additionally, it is important to note that the temperature dependence of the B_T anomaly is slightly different in MLMD and AIMD simulations. This is demonstrated by the B_T anomaly being weakened with temperature in MLMD, while it is independent of temperature in AIMD (see the inset of Fig. 6). We believe this difference is a result of the size effect, i.e., a small sample size is adapted in AIMD simulations, which has been revealed by our previous work on liquid potassium [18]. Also, the slight differences of B_T between MLIP and AIMD at low pressures, which may result from the size effect or limited performance of the machine learning potential in describing the high-order elastic constant, do not significantly reduce the reliability of our main findings.

C. Dynamic properties

Direct information on the dynamics of a system can be captured by the phonon band structures and VDOS obtained

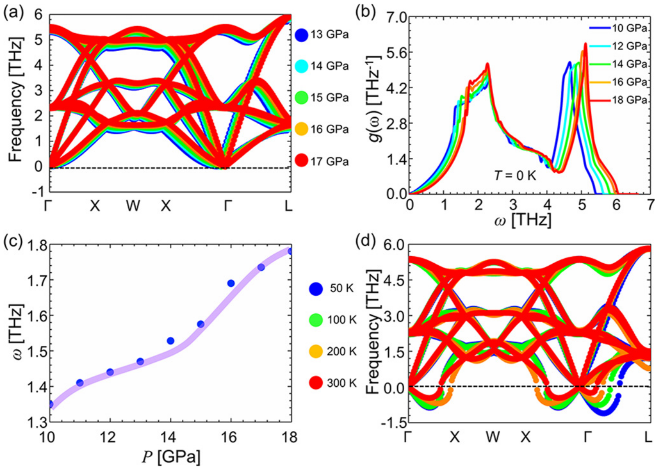

FIG. 7. Lattice vibration manner of face-centered cubic (fcc) potassium across electride transition. (a) Phonon dispersion of fcc structure at selected pressures and 0 K. (b) Pressures effect on the vibrational density of states (VDOS) at 0 K. (c) The frequency of shoulder at the first main peak (~1.5 THz) as a function of pressure. (e) Temperature effect on phonon dispersion at 14 GPa.

by lattice dynamics calculations [38]. Therefore, the phonon dispersions and the VDOSs of fcc potassium across the electride transition are calculated in Fig. 7. Figure 7(a) shows the phonon dispersions of fcc potassium from 13 to 17 GPa at 0 K, which is consistent with the clarifications of experiments and theoretical calculations that the fcc potassium is a stable phase in a wide of range pressures (~11.6 to ~20 GPa) [39,40]. Figure 7(b) shows the effect of pressure on the VDOSs of fcc potassium from DFT calculation at 0 K. Profiles of VDOSs with two main peaks show typical fcc structural features with a shoulder in the first peak (located ~1.5 THz) [41], and the shoulder gradually shifts to high frequency in addition to a sharp change between 14 and 16 GPa. This agrees well with the atom-to-electride transition. Furthermore, Fig. 7(c) shows the frequency of the shoulder at the first main peak as a function of pressure. We find an anomalous evolution of the frequency, i.e., a clear bump at ~16 GPa. This manner is like the abnormality shown in the isothermal bulk modulus (see Fig. 6). The phonon dispersion curves of different temperatures at 14 GPa are captured by the normal mode decomposition technique [34]. This method incorporates the phonon-electron coupling effect related to the electride state, equivalent to the nonanalytic terms in the model of Zhang *et al.* [19], which show imaginary frequencies due to the contribution of the electride, as shown in Fig. 7(d). We find that the density of the imaginary frequency is gradually enhanced when the temperature decreases. It is consistent with the model of Zhang *et al.* [19], which suggests that the imaginary frequency in electride materials is strongly correlated with the effective mass of ISQs.

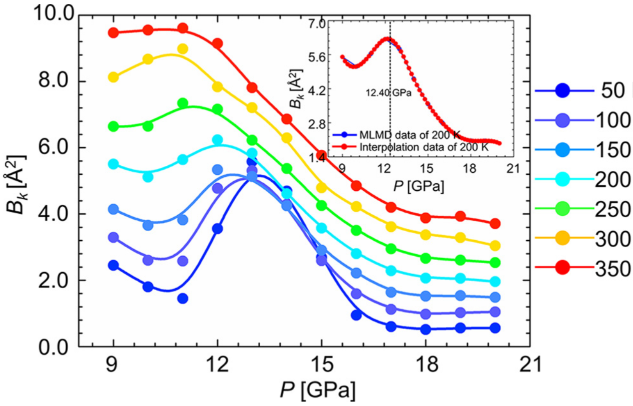

FIG. 8. Debye-Waller factor (B_k) of solid potassium from machine learning molecular dynamics (MLMD) simulation at different temperatures. It characterizes the effect of lattice vibrations as a function of pressure. The inset is the data points of B_k upon compression at 200 K, whose cubic spline interpolation is used to determine the maximum point of B_k.

The Debye-Waller factor (B_k), which characterizes the effect of lattice vibrations [42], is related to $\langle \mathbf{r}^2 \rangle$ or the mean square displacement, and $B_k = \frac{8\pi^2}{3}\langle r^2 \rangle$. Figure 8 shows the B_k of fcc potassium as a function of pressure along different isotherms ranging from 50 to 350 K. The B_k curves at low temperatures show an anomaly with a local maximum at ~14 GPa, which suggests that the amplitude of lattice vibrations is gradually enhanced across the atom-to-electride transition, like the effect of temperature [43]. The maximum points of B_k at various temperatures can be estimated from the cubic spline curve based on the MLMD data, as shown in the inset of Fig. 8. Interestingly, the anomaly in B_k of fcc potassium as a function of pressure gradually decays when the temperature rises and almost disappears at 350 K. In this aspect, it agrees well with the temperature-dependent thermodynamic properties of solid potassium in Figs. 4(a)–4(c).

IV. DISCUSSION

The focus of this paper is the anomalous behavior of a range of thermodynamic properties—specifically maxima and minima along isotherms which trace Widom lines in the *P-T* phase diagram. These thermodynamic anomalies can be understood using a two-state Bragg-Williams (BW)-type model to describe the electride transition under compression, which enables us to further understand the nature of the electride state. The BW model is a mean-field approximation to the Ising model [44], and here, the spins are mapped into the electride or electron states, and the field is mapped to the enthalpy difference between the two states. In this scenario, the excess Gibbs free energy due to the electride transition is

$$G_{\mathrm{ET}}(x) = x(U_e - PV_e - TS_e) + RT[x\ln x + (1-x)\ln(1-x)] + Jx(1-x), \quad (1)$$

where x is the electride fraction, U_e, S_e, and V_e are the difference in the internal energy, entropy, and volume between the normal and electride states, respectively, while J is a local coupling between electride and free electrons. These terms give immediate insight into the differences between free-electron and electride behavior. If J is repulsive, BW exhibits a solid-solid critical point at which all the thermodynamics anomalies converge; in potassium, we see no evidence of this, so we can assume that J is attractive. The electride is the high-pressure phase, so V_e must be positive. The free electron state is

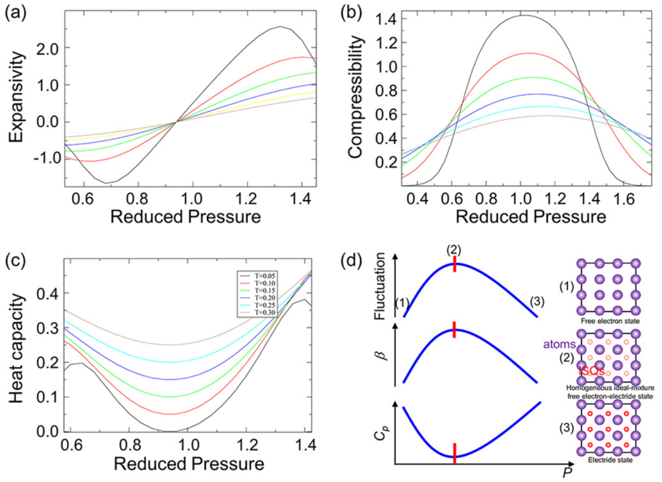

FIG. 9. Thermodynamic anomalies predicted by the Bragg-Williams-type model. Here, the parameters of the model are set as $U_e = 1.0$, $V_e = 1.0$, $J = -0.25$, and $S_e = 0.5$ in reduced units. (a) Thermal expansivity, (b) compressibility, and (c) heat capacity are calculated at different temperatures in reduced units. (d) A simplified picture of the correlation between thermal fluctuation induced by electride transition and anomalous thermodynamic responses.

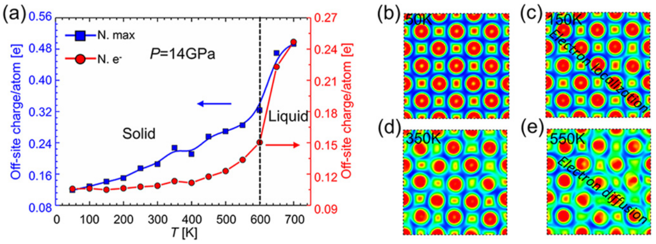

FIG. 10. Electronic properties of face-centered cubic (fcc) potassium during heating. (a) The frequency of off-atom Bader maxima (blue line) and average (red line) as a function of temperatures at 14 GPa. (b)–(e) Electron localization function (ELF) along (001) slices in simulation snapshots at 14 GPa and (50, 150, 350, 550 K). ELF values are shown in red, green, blue (RGB) scale from 0.0 (blue) to 0.7 (red).

stable at low P, T, so U_e must also be positive. Temperature dependence comes from both the TS_e term and the entropy of mixing.

The physical observables in BW including thermal expansivity, compressibility, and heat capacity can be calculated [45] as second derivatives of $\mathrm{Min}_x G\,(P, T)$ and are illustrated in Fig. 9. The BW model captures well the temperature dependence of these anomalies: C_p has two maxima and a minimum; β has a single maximum; α has a minimum and a maximum. Inspired by water [46,47], the maximum of compressibility (β) and the minimum of heat capacity (C_p) correspond to a maximum thermal fluctuation when the populations of electride and free-electron states are equal [see Fig. 9(d)]. Furthermore, the abnormalities become smaller while the temperature increases. All these features are consistent with our simulation results, which include both the excess free energy from the electride transition and the "normal" free energy from all other contributions, which we expect to be smoothly varying.

A particular feature of the BW model and the MLMD is the existence of a minimum in the heat capacity. In potassium, this moves to lower pressure as the temperature increases. The C_p minimum occurs when the crossover is primarily pressure driven and occurs where the two states have equal enthalpy. In fact, the BW contribution to the heat capacity comprises two broad maxima, but it is small compared with phonon contributions, and so the minimum between these broad maxima is the more easily seen feature. The negative slope shows that S_e is positive.

Furthermore, the electronic properties at various temperatures were calculated to understand the origin of the temperature effect. Figure 10(a) shows the temperature dependence of nonnuclear charge maxima and average value at 14 GPa. We find that both the maximum and averaged nonnuclear charge increase continuously with temperature before the melting point (T_m) and then soars into a high value after melting. It suggests a stronger electride nature of the liquid phase, consistent with our previous work [18]. The corresponding ELF topology at selected temperatures below T_m is shown in Figs. 10(b)–10(e). Noticeably, the nonnuclear ELF is more diffuse and spatially homogeneous at high temperatures [see Figs. 10(d) and 10(e)]. This is the origin of the weaken imaginary frequency of phonon dispersions as the temperature increases [see Fig. 7(d)], and it is quite different from the low temperature cases where the nonnuclear charge is more localized in the center of the interstitial lattice sites [see Figs. 10(b) and 10(c) and the 50 K curve at Fig. 7(d)] and behaves more like anions. The enhanced electron localization of HPE at low temperature may result in a stronger coupling of lattice vibrations between potassium ion cores and these ISQs [19], which is a response to the anomalies in fcc potassium under pressure. In contrast, the lattice fluctuation that is intensified at high temperatures can distort local structures randomly, thus missing the localization characteristics of ISQs. In this scenario, such delocalized nature may completely disappear when approaching the melting point, leading to the absence of thermophysical property abnormalities. We speculate that there may exist a high-order critical point at the crossing of the static and dynamic Schottky lines [47], which is very close to the bcc-fcc-liquid triple point, as shown in Fig. 1.

V. CONCLUSIONS

In summary, we have investigated the thermophysical properties across the atom-to-electride transition in fcc potassium utilizing large-scale MD simulations and *ab initio* calculations. We find that pure atom-to-electride transition in the solid phase without global structural phase change can still lead to thermodynamic and dynamic property anomalies under high pressure. It is due to the coupling of local structural dynamics with emerging ISQs upon compression. Additionally, the dependence of HPE on temperature gives rise to a weakening anomaly of thermophysical properties at high temperatures. We suggest that the effect of the atom-to-electride transition on the thermophysical properties cannot be underestimated in alkali metals and other materials that undergo electride transition under high pressure.

ACKNOWLEDGMENTS

This paper was supported by the National Natural Science Foundation of China (No. 51320105014, No. 51871177, and No. 51931004), the 111 project 2.0 (No. BP2018008), the ERC grant "Hecate," and the China Postdoctoral Science Foundation (No. 2020M673385).

---

[1] E. Wigner and F. Seitz, On the constitution of metallic sodium, Phys. Rev. **43**, 804 (1933).

[2] F. S. Ham, Energy bands of alkali metals. I. Calculated bands, Phys. Rev. **128**, 82 (1962).

[3] E. Gregoryanz, L. F. Lundegaard, M. I. McMahon, C. Guillaume, R. J. Nelmes, and M. Mezouar, Structural diversity of sodium, Science **320**, 1054 (2008).

[4] C. L. Guillaume, E. Gregoryanz, O. Degtyareva, M. I. McMahon, M. Hanfland, S. Evans, M. Guthrie, S. V. Sinogeikin, and H. K. Mao, Cold melting and solid structures of dense lithium, Nat. Phys. **7**, 211 (2011).

[5] R. Boehler and C. S. Zha, Systematics in the melting behavior of the alkali-metals from dac measurements, Physica B&C **139**, 233 (1986).

[6] M. I. McMahon and R. J. Nelmes, High-pressure structures and phase transformations in elemental metals, Chem. Soc. Rev. **35**, 943 (2006).

[7] S. Falconi, M. I. McMahon, L. F. Lundegaard, C. Hejny, R. J. Nelmes, and M. Hanfland, X-ray diffraction study of diffuse scattering in incommensurate rubidium-IV, Phys. Rev. B **73**, 214102 (2006).

[8] B. Rousseau and N. W. Ashcroft, Interstitial Electronic Localization, Phys. Rev. Lett. **101**, 046407 (2008).

[9] Y. M. Ma, M. Eremets, A. R. Oganov, Y. Xie, I. Trojan, S. Medvedev, A. O. Lyakhov, M. Valle, and V. Prakapenka, Transparent dense sodium, Nature (London) **458**, 182 (2009).

[10] J. L. Dye, Electrons as anions, Science **301**, 607 (2003).

[11] M. Gatti, I. V. Tokatly, and A. Rubio, Sodium: A Charge-Transfer Insulator at High Pressures, Phys. Rev. Lett. **104**, 216404 (2010).

[12] M. Marques, M. Santoro, C. L. Guillaume, F. A. Gorelli, J. Contreras-Garcia, R. T. Howie, A. F. Goncharov, and E. Gregoryanz, Optical and electronic properties of dense sodium, Phys. Rev. B **83**, 184106 (2011).

[13] T. Matsuoka and K. Shimizu, Direct observation of a pressure-induced metal-to-semiconductor transition in lithium, Nature (London) **458**, 186 (2009).

[14] C. J. Pickard and R. J. Needs, Dense Low-Coordination Phases of Lithium, Phys. Rev. Lett. **102**, 146401 (2009).

[15] M. Marques, M. I. McMahon, E. Gregoryanz, M. Hanfland, C. L. Guillaume, C. J. Pickard, G. J. Ackland, and R. J. Nelmes, Crystal Structures of Dense Lithium: A Metal-Semiconductor-Metal Transition, Phys. Rev. Lett. **106**, 095502 (2011).

[16] G. A. Adebayo, *Ab initio* calculations of optical properties of Li and K at high pressures, J. Phys. Chem. Solids **74**, 1221 (2013).

[17] Z. Yu, H. Y. Geng, Y. Sun, and Y. Chen, Optical properties of dense lithium in electride phases by first-principles calculations, Sci. Rep. **8**, 3868 (2018).

[18] H. X. Zong, V. N. Robinson, A. Hermann, L. Zhao, S. Scandolo, X. D. Ding, and G. J. Ackland, Free electron to electride transition in dense liquid potassium, Nat. Phys. **17**, 955 (2021).

[19] L. L. Zhang, H. Y. Geng, and Q. Wu, Prediction of anomalous LA-TA splitting in electrides, Matter Radiat. Extrem. **6**, 038403 (2021).

[20] V. N. Robinson, H. X. Zong, G. J. Ackland, G. Woolman, and A. Hermann, On the chain-melted phase of matter, Proc. Natl. Acad. Sci. USA **116**, 10297 (2019).

[21] L. Zhao, H. X. Zong, X. D. Ding, J. Sun, and G. J. Ackland, Commensurate-incommensurate phase transition of dense potassium simulated by machine-learned interatomic potential, Phys. Rev. B **100**, 220101 (2019).

[22] G. Boucher, First-Principles Study of the Phase Diagram of Potassium, Ph.D. thesis, University College London, 2019.

[23] E. E. McBride, K. A. Munro, G. W. Stinton, R. J. Husband, R. Briggs, H. P. Liermann, and M. I. McMahon, One-dimensional chain melting in incommensurate potassium, Phys. Rev. B **91**, 144111 (2015).

[24] M. Sakata, Y. Nakamoto, T. Matsuoka, Y. Ohishi, and K. Shimizu, Structural phase transition of potassium under high-pressure and low-temperature condition, J. Phys.: Conf. Ser. **950**, 042020 (2017).

[25] G. Kresse and J. Furthmuller, Efficiency of ab-initio total energy calculations for metals and semiconductors using a plane-wave basis set, Comput. Mater. Sci. **6**, 15 (1996).

[26] G. Kresse and J. Furthmuller, Efficient iterative schemes for ab initio total-energy calculations using a plane-wave basis set, Phys. Rev. B **54**, 11169 (1996).

[27] B. Schölkopf and A. J. Smola, *Learning with Kernels* (MIT Press, Cambridge, 2002).

[28] A. Samanta, M. E. Tuckerman, T. Q. Yu, and E. Weinan, Microscopic mechanisms of equilibrium melting of a solid, Science **346**, 729 (2014).

[29] S. Nose, A unified formulation of the constant temperature molecular-dynamics methods, J. Chem. Phys. **81**, 511 (1984).

[30] S. Plimpton, Fast parallel algorithms for short-range molecular-dynamics, J. Comput. Phys. **117**, 1 (1995).

[31] K. Momma and F. Izumi, VESTA 3 for three-dimensional visualization of crystal, volumetric and morphology data, J. Appl. Cryst. **44**, 1272 (2011).

[32] J. P. Perdew, J. A. Chevary, S. H. Vosko, K. A. Jackson, M. R. Pederson, D. J. Singh, and C. Fiolhais, Atoms, molecules, solids, and surfaces—applications of the generalized gradient approximation for exchange and correlation, Phys. Rev. B **46**, 6671 (1992).

[33] A. Togo and I. Tanaka, First principles phonon calculations in materials science, Scr. Mater. **108**, 1 (2015).

[34] A. Carreras, A. Togo, and I. Tanaka, DYNAPHOPY: A code for extracting phonon quasiparticles from molecular dynamics simulations, Comput. Phys. Commun. **221**, 221 (2017).

[35] G. Henkelman, A. Arnaldsson, and H. Jonsson, A fast and robust algorithm for Bader decomposition of charge density, Comput. Mater. Sci. **36**, 354 (2006).

[36] A. D. Becke and K. E. Edgecombe, A simple measure of electron localization in atomic and molecular-systems, J. Chem. Phys. **92**, 5397 (1990).

[37] S. Ayrinhac, V. N. Robinson, F. Decremps, M. Gauthier, D. Antonangeli, S. Scandolo, and M. Morand, High-pressure transformations in liquid rubidium, Phys. Rev. Mater. **4**, 113611 (2020).

[38] D. Alfe, PHON: A program to calculate phonons using the small displacement method, Comput. Phys. Commun. **180**, 2622 (2009).

[39] G. Woolman, V. N. Robinson, M. Marques, I. Loa, G. J. Ackland, and A. Hermann, Structural and electronic properties of the alkali metal incommensurate phases, Phys. Rev. Mater. **2**, 053604 (2018).

[40] O. Narygina, E. E. McBride, G. W. Stinton, and M. I. McMahon, Melting curve of potassium to 22 GPa, Phys. Rev. B **84**, 054111 (2011).

[41] D. Srivastava, U. V. Waghmare, and S. K. Sarkar, Evidence of scaling in the high pressure phonon dispersion relations of some elemental solids, J. Chem. Phys. **141**, 044714 (2014).

[42] S. Caravati, M. Bernasconi, T. D. Kuhne, M. Krack, and M. Parrinello, First-principles study of crystalline and amorphous $Ge_2Sb_2Te_5$ and the effects of stoichiometric defects, J. Phys.: Condens. Matter **21**, 255501 (2009).

[43] C. M. Roland and K. L. Ngai, The anomalous Debye-Waller factor and the fragility of glasses, J. Chem. Phys. **104**, 2967 (1996).

[44] W. L. Bragg and E. J. Williams, The effect of thermal agitation on atomic arrangement in alloys, Proc. Roy. Soc. London, Ser. A **151**, 699 (1934).

[45] G. J. Ackland, H. Zong, V. N. Robinson, S. Scandolo, and A. Hermann, Two-state model for critical points and the negative slope of the melting curve, Phys. Rev. B **104**, 054120 (2021).

[46] A. Nilsson and L. G. M. Pettersson, The structural origin of anomalous properties of liquid water, Nat. Commun. **6**, 8998 (2015).

[47] R. Shi and H. Tanaka, The anomalies and criticality of liquid water, Proc. Natl. Acad. Sci. USA **117**, 26591 (2020).